


Cite this: *RSC Adv.*, 2018, 8, 42100

Color tuning and white light emission by codoping in isostructural homochiral lanthanide metal–organic frameworks†

Wenbo Wang,^a Ruiying Wang,^b Yafang Ge^a and Benlai Wu[✉] 

Four lanthanide-based homochiral metal–organic frameworks (Ln-HMOFs), {[Ln₂(HL)₂(H₂O)₄]·2Cl·5H₂O}_n [Ln = Gd (1), Eu (2), Tb (3) and Dy (4)], have been synthesized through solvothermal reactions of chiral ligand (S)-5-(((1-carboxyethyl)amino)methyl)isophthalic acid (H₃L) with corresponding LnCl₃·6H₂O. They are binodal (3,6)-connected frameworks with kgd nets based on binuclear cluster units and zwitterionic (HL)^{2−} linkers. Considering the isostructuralism of these Ln-HMOFs as well as the blue emission of compound 1 and the strong typical Eu³⁺ and Tb³⁺ emissions of compounds 2 and 3, single-phase mixed-lanthanide HMOFs have been prepared by doping of Ln³⁺ into the Ln-HMOFs to modulate light-emitting color. Interestingly, the bimetallic doped Eu/Tb-HMOFs [(Eu_xTb_{1−x})₂(HL)₂(H₂O)₄]·2Cl·5H₂O display a fluent change of light-emitting color among green, yellow, orange, orange-red, and red by adjusting the doping concentration of Eu³⁺ ions into the Tb-HMOF. Very importantly, the trimetallic doped Eu/Gd/Tb-HMOF [(Eu_{0.1388}Gd_{0.6108}Tb_{0.2504})₂(HL)₂(H₂O)₄]·2Cl·5H₂O emits white light upon excitation at 355 nm, whose emission can also be switched between different colors when excited with different ultraviolet light. Furthermore, the fluorescence response of Tb-HMOF to various usual metal ions, and especially fluorescent sensing behaviours to Fe³⁺, Cr³⁺ and Al³⁺ have been preliminarily investigated.

Received 13th August 2018

Accepted 13th December 2018

DOI: 10.1039/c8ra06793g

rsc.li/rsc-advances

Introduction

Further motivated by a longing for greener, safer and energy efficient light-emitting materials, the exploration of solid-state luminescent materials through various approaches including metal-doped or hybrid inorganic materials,^{1–3} organic molecules,⁴ polymers,⁵ nanomaterials,⁶ and metal complexes¹ has evolved rapidly in recent years. Lanthanide metal–organic frameworks (Ln-MOFs) owing to their tunable structure diversities,^{7,8} attractive photophysical properties, and potential applications in biomedical imaging,⁹ lighting,¹⁰ and display devices⁷ make them promising candidates for the development of high-efficiency light-emitting materials. As is well known, lanthanide ions feature excellent luminescence properties such as long lifetime, large Stokes shift and narrow-band but the weak light absorption caused by Laporte forbidden f–f transitions makes the direct lanthanide excitation inefficient.¹¹ However, Ln-MOFs incorporating Ln³⁺ with judiciously selected organic linkers which can

participate in efficient light absorption and ligand-to-metal energy-transfer processes through the so-called “antenna effect” can possibly overcome this paucity.^{12–14} Additionally, the self-assemblies of varied Ln³⁺ ions with the same organic bridges under the same reaction conditions always result in isostructural Ln-MOFs due to very similar coordination environments of Ln³⁺ ions, which provides a facile platform for color tuning and white light emission through the doping of different Ln³⁺ ions into isostructural MOFs without disruption of the original structure.^{15–19} Currently, aromatic polycarboxylate ligands have been well explored in the formation of Ln-MOFs luminescence materials, not only because their carboxyl moieties can adopt multiple coordination modes to give high-dimensional unique structures with good thermal stability, but also because they can increase light absorption, provide blue color sources, and act as excellent sensitizers to activate Ln³⁺ ions.^{20–24}

Homochiral metal–organic frameworks (HMOFs) have attracted special attention owing to their fascinating structures and intriguing potential applications in asymmetric catalysis and enantioselective separation.^{25–33} In contrast, studies on lanthanide-based homochiral metal–organic frameworks (Ln-HMOFs) as multicolor luminescence materials are still quite limited at present, although they have unique optical properties, such as nonlinear optics, circular dichroism and chiral polarized photoemission,^{16,34–37} which could further expand its application in luminescent materials. Herein, (S)-5-(((1-carboxyethyl)amino)methyl)isophthalic acid (H₃L, Scheme 1), a typical

^aCollege of Chemistry and Molecular Engineering, Zhengzhou University, Zhengzhou 450001, P. R. China. E-mail: wbl@zzu.edu.cn; Tel: +86 0371 67783126

^bSchool of Chemical Engineering, Henan Vocational College of Applied Technology, Zhengzhou 450042, P. R. China

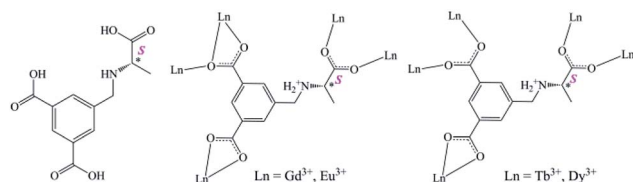
† Electronic supplementary information (ESI) available: Additional figures and tables, TGA, PXRD, IR spectra, excitation and emission spectra, decay curves (PDF)s. CCDC 1852703–1852706 for 1–4. For ESI and crystallographic data in CIF or other electronic format see DOI: 10.1039/c8ra06793g

aromatic polycarboxylate linker being synthesized and used in our recent fabrication of novel transition metal HMOFs where H_3L ligand displays various existing forms and versatile coordination models and also transmits its chirality into the whole frameworks,³⁸ was selected as a chiral bridge and sensitizer to construct Ln-HMOFs. We report the preparation of isostructural Ln-HMOFs, $\{[Ln_2(HL)_2(H_2O)_4] \cdot 2Cl \cdot 5H_2O\}_n$ [$Ln = Gd$ (1), Eu (2), four Tb (3) and Dy (4)], and a series of single-phase mixed-lanthanide HMOFs analogues. More importantly, color tuning and white light-emission can be easily attained by carefully adjusting the relative concentration of lanthanum ions in the resulting 2D Ln-HMOFs. Furthermore, crystal structure, circular dichroism, luminescent mechanism, color tuning, and cation sensing have been investigated in detail.

Experiment

Materials and general procedures

All the reagents were of analytical grade and obtained from commercial sources without further purification. Enantiopure ligand (*S*)-5-(((1-carboxyethyl)amino)methyl)isophthalic acid (H_3L) were prepared according to our reported procedure.³⁸ Elemental analyses were performed with a Carlo-Erba 1106 elemental analyzer. IR spectra (KBr pellets) were recorded in the range 400–4000 cm^{-1} on a Nicolet NEXUS 470 FT-IR spectrophotometer (Fig. S1†). Thermal analysis curves were scanned from 30 to 800 °C under air on a STA 409 PC thermal analyzer (Fig. S2†). X-ray diffraction (PXRD) patterns of the samples were recorded on a RIGAKU-DMAX2500 X-ray diffractometer with $Cu K\alpha$ radiation (Fig. S3–S4†). The luminescence spectra for the solid and suspension samples were determined at room temperature on a Hitachi F-4500 fluorophotometer with a xenon arc lamp as light source. The fluorescence lifetime τ was determined by a FLS980 fluorescence spectrometer. The emission quantum yield measurements were carried out on solid samples using an integrating sphere on an Edinburgh FLS980 fluorescence spectrometer. Solid-state circular dichroism (CD) spectra (KBr pellets) were recorded at room temperature on a MOS-450 spectrometer. Inductively coupled plasma (ICP) spectroscopy was detected on a Thermo ICAP 6000 DUO spectrometer. On the basis of international CIE standards, the Commission International de l'Eclairage (CIE) color coordinates were calculated. The general colour rendering index (CRI) were designated by the symbol R_a , which is the average value of R_1 to R_8 .^{39,40} The numbers in parentheses indicate the Munsell colour system.⁴¹ The correlated colour temperature (CCT) values were obtained based on the corresponding CIE colour coordinates.



Scheme 1 Schematic representation of chiral ligand H_3L and the coordination modes of its zwitterionic $(HL)^{2-}$ in 1–4.

Synthesis of compounds

All compounds including the mixed-lanthanide ones were synthesized in a similar procedure except for the different starting lanthanide salts. The synthesis of $\{[Gd_2(HL)_2(H_2O)_4] \cdot 2Cl \cdot 5H_2O\}_n$ (1) is detailedly introduced as a representative: a mixture of H_3L (0.0134 g, 0.05 mmol), $GdCl_3 \cdot 6H_2O$ (0.0183 g, 0.05 mmol), deionized H_2O (0.5 mL) and acetonitrile (2 mL) was sealed in a 25 mL Teflon-lined stainless autoclave and heated at 120 °C for 24 h. After the mixture was cooled to room temperature at a rate of 5 °C h^{-1} , colorless block crystals were obtained, washed with distilled water, and dried in air, resulting in 62% yield (based on Gd). Anal. calcd for $C_{24}H_{40}Cl_2Gd_2N_2O_{21}$ (%): C, 26.74; H, 3.74; N, 2.60. Found: C, 26.58; H, 3.75; N, 2.58. IR (KBr, cm^{-1}): 3439 (m), 2960 (w), 1641 (s), 1553 (s), 1534 (s), 1451 (s), 1395 (s), 1249 (w), 1116 (w), 816 (w) 780 (s), 732 (s).

$\{[Eu_2(HL)_2(H_2O)_4] \cdot 2Cl \cdot 5H_2O\}_n$ (2). Yield 62% (based on Gd). Anal. calcd for $C_{24}H_{40}Cl_2Eu_2N_2O_{21}$ (%): C, 27.01; H, 3.78; N, 2.62. Found: C, 26.90; H, 3.81; N, 2.65. IR (KBr, cm^{-1}): 3428 (m), 2981 (w), 1640 (s), 1552 (s), 1534 (s), 1449 (s), 1393 (s), 1249 (w), 1112 (w), 815 (w) 781 (s), 731 (s).

$\{[Tb_2(HL)_2(H_2O)_4] \cdot 2Cl \cdot 5H_2O\}_n$ (3). Yield 64% (based on Tb). Anal. calcd for $C_{24}H_{40}Cl_2N_2O_{21}Tb_2$ (%): C, 26.66; H, 3.73; N, 2.59. Found: C, 26.44; H, 3.75; N, 2.61. IR (KBr, cm^{-1}): 3443 (m), 2952 (w), 1643 (s), 1548 (s), 1539 (s), 1457 (s), 1396 (s), 1250 (w), 1114 (w), 816 (w) 780 (s), 733 (s).

$\{[Dy_2(HL)_2(H_2O)_4] \cdot 2Cl \cdot 5H_2O\}_n$ (4). Yield 65% (based on Dy). Anal. calcd for $C_{24}H_{40}Cl_2Dy_2N_2O_{21}$ (%): C, 26.48; H, 3.70; N, 2.57. Found: C, 26.37; H, 3.73; N, 2.56. IR (KBr, cm^{-1}): 3430 (m), 2952 (w), 1646 (s), 1550 (s), 1540 (s), 1456 (s), 1397 (s), 1249 (w), 1111 (w), 818 (w) 782 (s), 732 (s).

As for the isostructural mixed-lanthanide analogues, Eu^{3+}/Tb^{3+} or $Eu^{3+}/Gd^{3+}/Tb^{3+}$ codoped compounds adopt the same methods as those mentioned above just by adding the corresponding $LnCl_3 \cdot 6H_2O$ ($Ln^{3+} = Gd^{3+}, Eu^{3+}$ or Tb^{3+}) as the starting materials in different stoichiometric ratios. Their structure and purity were confirmed by PXRD (Fig. S4†), IR spectra (Fig. S1†), and elemental analyses (ICP) (Table S1†).

Luminescence sensing experiments

A ground sample (10 mg) of the Tb-HMOF was dispersed in an aqueous solution (3 mL) of $M(NO_3)_x$ ($M^{x+} = Na^+, K^+, Ag^+, Cd^{2+}, Ba^{2+}, Mg^{2+}, Mn^{2+}, Ni^{2+}, Zn^{2+}, Cu^{2+}, Co^{2+}, Hg^{2+}, Pb^{2+}, Fe^{3+}, Al^{3+}$, or Cr^{3+} , 1×10^{-3} mol L^{-1}) which was ultrasonicated for 30 min at room temperature. The resulted mixtures were used for luminescent measurements.

X-ray structure determination

On a Bruker APEX-II CCD diffractometer, single-crystal X-ray data of 1–4 were collected at 293(2) K using graphite-monochromated $Mo K\alpha$ radiation ($\lambda = 0.71073$ Å). Absorption corrections were applied by using the multiscan program SADABS.⁴² The structures were solved by direct methods and refined on F^2 full-matrix least-squares using the SHELXTL program package.^{43,44} All of the non-hydrogen atoms were refined with anisotropic displacement parameters during the



final cycles. The H atoms attached to C were generated geometrically while the H atoms attached to O and N were located from different Fourier maps and treated as idealized contributions. Unluckily, the H atoms of some water molecules were not added owing to not suitable Fourier maps being picked up. Notably, the precision of the C–C bonds of 2–4 is slightly low, which perhaps results from the weak diffractions owing to the bad quality and small sizes of the single crystals and/or from the effects of heavy Ln atoms whose strong diffraction signals affect the accurate detection of lighter atoms C. Further attempts to get suitable single crystals by different methods as well as the recollecting crystal data at a lower temperature were of fail. The crystal data were summarized in Table 1, and the selected bond distances were given in Table S2.†

Results and discussion

Synthesis and general characterization of compounds

The isostructural Ln-HMOFs including the mixed-lanthanide species were solvothermally synthesized at 120 °C using the corresponding $\text{LnCl}_3 \cdot 6\text{H}_2\text{O}$ and the chiral ligand H_3L in a mixed solvent of deionized H_2O and acetonitrile. The crystalline products are air-stable and insoluble in water or any common organic solvents.

The chemical formulas of single-lanthanide compounds 1–4 have been confirmed by satisfactory elemental analysis and single-crystal X-ray diffraction. In the IR spectra of 1–4, the strong and broad absorption bands in a range of 3400–3500 cm^{-1} indicates the presence of $\nu_{\text{N-H}}$ and the $\nu_{\text{O-H}}$ stretching frequencies of amino groups and water molecules, respectively. Four complexes exhibit strong characteristic absorptions around 1534–1646 cm^{-1} for $\nu_{\text{as}}(-\text{COO}^-)$ and 1393–1457 cm^{-1} for $\nu_{\text{s}}(-\text{COO}^-)$, respectively. However, no strong characteristic absorptions around 1700 cm^{-1} for $(-\text{COOH})$ were observed, being in agreement with the single-crystal X-ray diffraction analysis results that all carboxyl groups of ligand H_3L in compounds 1–4 were deprotonated. The accurate molar ratios of the individual lanthanide elements in the mixed-

lanthanide compounds have been determined by inductively coupled plasma (ICP) spectroscopy (Table S1†), being well consistent with the corresponding ratios in the starting mixture. The phase purities and isostructuralism of all the as-synthesized Ln-HMOFs have been verified by powder X-ray diffraction (PXRD) measurements. Clearly, the experimental PXRD patterns of single-lanthanide compounds 1–4 are very similar to each other and match well with those simulated, indicating the phase purities and isostructuralism of those polycrystalline samples (Fig. S3†). Meanwhile, the observed PXRD patterns of all the bi- and tri-metallic doped samples are in conformity to the simulated pattern of 1 (Fig. S4†), demonstrating that they are isostructural with single-lanthanide compounds 1–4. Single-lanthanide compounds 1–4 all experience a very similar three-stepped thermal decomposition behavior revealed by TGA (Fig. S2†). The first weight loss corresponds to the removal of five lattice water molecules (calcd. 8.36%, obsd. 7.70% for 1; calcd. 8.44%, obsd. 7.60% for 2; calcd. 8.33%, obsd. 8.23% for 3; calcd. 8.28%, obsd. 7.65% for 4) before 130, 135, 150, and 155 °C, respectively. The second weight loss occurs in a temperature range of 155–230 °C, being attributable to the release of four coordinated water molecules (calcd. 6.68%, obsd. 6.60% for 1; calcd. 6.75%, obsd. 6.62% for 2; calcd. 6.66%, obsd. 6.10% for 3; calcd. 6.62%, obsd. 6.07% for 4). The removal of the organic components (calcd. 51.33%, obsd. 48.65% for 1; calcd. 51.84%, obsd. 48.02% for 2; calcd. 51.17%, obsd. 48.84% for 3; calcd. 50.83%, obsd. 49.45% for 4) occurred in a temperature range of 300–700 °C. The final residue for each complex corresponds to the formation of the respective lanthanide oxide. In addition, the thermal decomposition behavior of the trimetallic doped sample has been also investigated as a representative of the mixed-lanthanide species, and the result shows that its thermal decomposition behavior (weight loss and decomposition temperature) is surprisingly similar to that of all single-lanthanide compounds (Fig. S2†). The TGA results show that these single- and mixed-lanthanide frameworks have higher thermal stabilities being suitable for potential applications in

Table 1 Crystal data and structure refinement for 1–4

Compounds	1	2	3	4
Formula	$\text{C}_{24}\text{H}_{40}\text{Cl}_2\text{Gd}_2\text{N}_2\text{O}_{21}$	$\text{C}_{24}\text{H}_{40}\text{Cl}_2\text{Eu}_2\text{N}_2\text{O}_{21}$	$\text{C}_{24}\text{H}_{40}\text{Cl}_2\text{Tb}_2\text{N}_2\text{O}_{21}$	$\text{C}_{24}\text{H}_{40}\text{Cl}_2\text{Dy}_2\text{N}_2\text{O}_{21}$
Temp (K)	293(2)	293(2)	293(2)	293(2)
Formula weight	1077.98	1067.40	1081.32	1088.48
Crystal system	Triclinic	Triclinic	Triclinic	Triclinic
Space group	<i>P</i> 1	<i>P</i> 1	<i>P</i> 1	<i>P</i> 1
<i>a</i> (Å)	9.6682(6)	9.6686(6)	9.6763(4)	9.6947(4)
<i>b</i> (Å)	10.0302(6)	10.0202(4)	10.0338(4)	10.0533(5)
<i>c</i> (Å)	10.9110(7)	10.8727(4)	10.9853(5)	11.0032(7)
$\alpha/^\circ$	104.893(2)	104.824(3)	105.072(3)	105.039(5)
$\beta/^\circ$	93.675(2)	93.710(5)	93.691(3)	93.823(4)
$\gamma/^\circ$	110.003(2)	109.569(5)	110.107(4)	110.052(4)
<i>V</i> (Å ³)	947.30(10)	946.31(8)	953.10(7)	958.48(9)
<i>Z</i> , ρ_{calcd} (g cm ^{−3})	1, 1.890	1, 1.873	1, 1.884	1, 1.886
GOF	1.061	1.052	1.060	1.051
Flack parameter	0.195(8)	0.20(3)	0.25(2)	0.22(2)
<i>R</i> 1, <i>wR</i> 2 (<i>I</i> > 2 σ (<i>I</i>))	0.0164, 0.0427	0.0603, 0.1298	0.0415, 0.0804	0.0467, 0.0840
Largest diff. peak and hole	0.668, −0.517	3.370, −2.031	0.994, −0.778	1.159, −0.985



solid-state luminescence materials, and again confirm the number of lattice and coordinated water molecules in their chemical formulas.

Crystal structure descriptions

Structures of $\{[\text{Ln}_2(\text{HL})_2(\text{H}_2\text{O})_4] \cdot 2\text{Cl} \cdot 5\text{H}_2\text{O}\}_n$ [$\text{Ln} = \text{Gd}$ (1), Eu (2), Tb (3) and Dy (4)]. Four single-lanthanide compounds 1–4 were determined crystallographically. They are isostructural with the same chiral space group $P1$, and feature the dinuclear cluster-based 2D networks. Though the check results using PLATON suggest that there is a possibly higher pseudosymmetry $P\bar{1}$ in their structural models, this can be due to the pseudotranslation symmetry of heavy Ln atoms.^{45,46} Their chirality was further confirmed by the solid-state CD spectra (*vide infra*). As a representative case, only the crystal structure of 1 is herein discussed in detailed. The asymmetric unit of 1 consists of two $(\text{HL})^{2-}$ ligands, two independent Gd^{3+} ions, four coordinated water molecules, five lattice water molecules, and two free Cl^- . Gd1 and Gd2 are nine-coordinated by seven O atoms from two chelating carboxylates and three bridging carboxylates of five different $(\text{HL})^{2-}$ ligands and two O atoms from water molecules, respectively, forming distorted single-capped square antiprism (C_{4v}) polyhedron configurations (Fig. 1a). The Gd–O bond lengths vary from 2.310(8) Å to 2.925(8) Å, which corresponds to those reported for other lanthanide–oxygen donor complexes,⁴⁷ and the O–Gd–O angles range from 47.4(2) to 148.2(3)°. Every H_3L ligand in 1, with its three carboxyls being completely deprotonated and meanwhile its amino group being protonated, exists in a zwitterionic form of $(\text{HL})^{2-}$ as observed in its Pb–HMOF.³⁸ Interestingly, the three carboxylate groups of $(\text{HL})^{2-}$ adopt three different coordination modes, namely, chelating fashion $\mu_1 - \eta^1:\eta^1$, chelating and

bridging fashion $\mu_2 - \eta^2:\eta^1$, and bridging fashion $\mu_2 - \eta^1:\eta^1$, unlike to those found in its transition metal frameworks.³⁸ Consequently, ligand $(\text{HL})^{2-}$ acts as a κ_7 -linker to connect five Gd^{3+} ions.

Notably, the two independent Gd^{3+} ions are connected by four carboxylate groups from four $(\text{HL})^{2-}$ ligands to form a binuclear cluster $[\text{Gd}_2(\text{COO})_4]$ (Fig. 1b), which is connected by $(\text{HL})^{2-}$ to produce a wave-like homochiral layer paralleling to ab plane (Fig. 1c). In the layer, each $(\text{HL})^{2-}$ ligand bonds three $[\text{Gd}_2(\text{COO})_4]$ units. Topologically, the $(\text{HL})^{2-}$ ligand and $[\text{Gd}_2(\text{COO})_4]$ unit can be considered as 3- and 6-connected nodes, respectively. Thus, the whole framework of 1 can be described as a (3,6)-connected kgd net with point (Schläfli) symbol of $(4^3)_2(4^6.6^6.8^3)$ [Fig. 2]. Those layers stack up along c axis with their chiral aminopropionate groups arraying up and down. Moreover, every protonated amino group of $(\text{HL})^{2-}$ ligand hydrogen-bonds two independent chloride anions (Cl1 and Cl2) which are further hydrogen-bonded by another amino group from the adjacent layer, and in such a way it results in an interesting 3D porous homochiral pillared-layer supramolecular framework with lattice water molecules in apertures when regarded the hydrogen-bonded (N_2Cl_2) rings as pillars (Fig. 3).

It should be mentioned that with the radium decrease of Ln atoms the κ_7 -linker $(\text{HL})^{2-}$ in 1 and 2 becomes the κ_6 -linker $(\text{HL})^{2-}$ in 3 and 4 owing to the chelating and bridging fashion $\mu_2 - \eta^2:\eta^1$ of the carboxylate becoming the bridging fashion $\mu_2 - \eta^1:\eta^1$ (Scheme 1, Fig. S5–S7†). As a result, both Tb^{3+} in 3 and Dy^{3+} in 4 adopt eight-coordinated slightly distorted square antiprism (C_{4v}) polyhedron configurations (Fig. S6–S7†). In their binuclear clusters $[\text{Tb}_2(\text{COO})_4]$ and $[\text{Dy}_2(\text{COO})_4]$, the bridging model between the two metal centers is slightly different from that found in the binuclear clusters $[\text{Gd}_2(\text{COO})_4]$ and $[\text{Eu}_2(\text{COO})_4]$ (Fig. 1 and S5–S7†).

Solid-state circular dichroism (CD) studies

To further demonstrate their homochirality, solid-state CD spectra of 1–4 have been measured with KBr pellets (Fig. 4). In

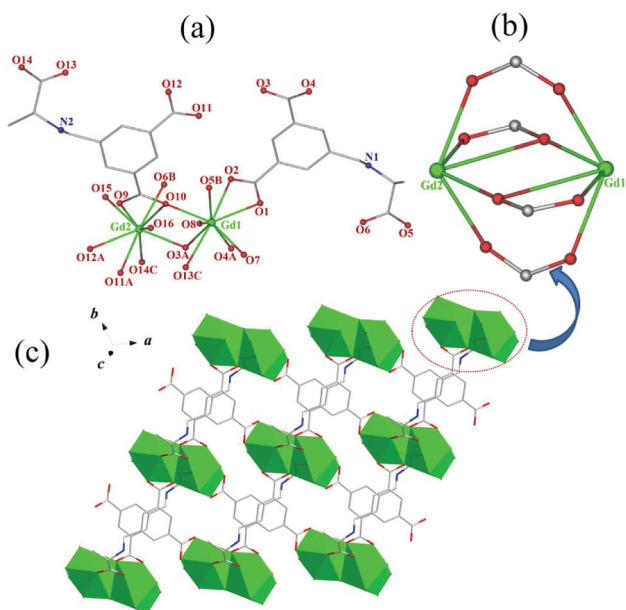


Fig. 1 (a) Coordination geometries of Gd^{3+} in 1; (b) binuclear cluster $[\text{Gd}_2(\text{COO})_4]$ unit; (c) wave-like homochiral layer structure of 1 based on binuclear cluster units $[\text{Gd}_2(\text{COO})_4]$ and zwitterionic $(\text{HL})^{2-}$ linkers. Symmetry code: (A) $x, 1 + y, z$; (B) $-1 + x, y, z$; (C) $1 + x, 1 + y, z$.

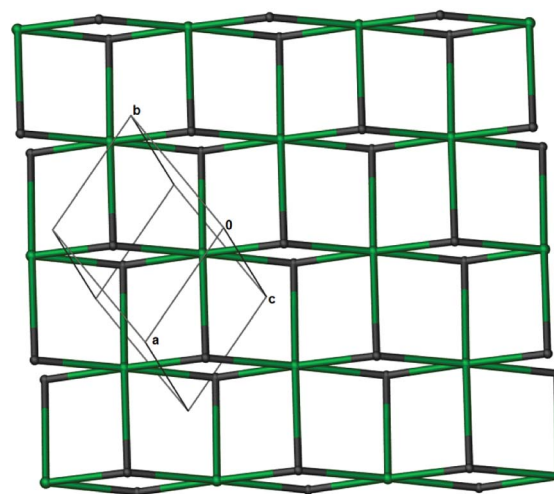


Fig. 2 Schematic representation of 2D (3,6)-connected kgd topology of 1.



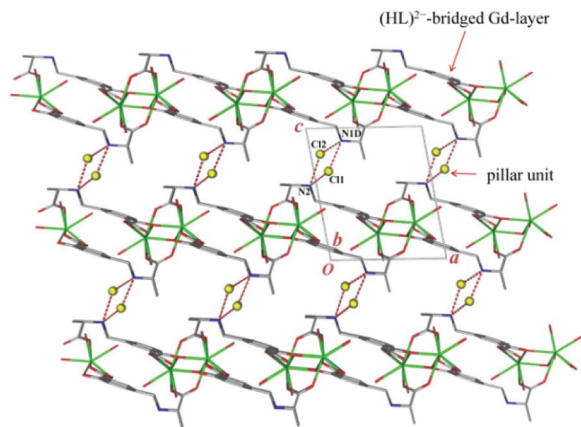


Fig. 3 View of interesting 3D porous homochiral pillared-layer supramolecular framework of **1**, regarding the hydrogen-bonded (N_2Cl_2) rings as pillars ($\text{N}2\cdots\text{Cl}1 = 3.209(10)$ Å, $\text{N}2\cdots\text{Cl}2 = 3.071(9)$ Å, $\text{N}1\text{D}\cdots\text{Cl}1 = 3.129(9)$ Å, $\text{N}1\text{D}\cdots\text{Cl}2 = 3.210(10)$ Å; lattice water molecules in apertures were omitted for clarity). Symmetry code: (D) $-1 + x, y, 1 + z$.

their CD spectra, obvious chiroptical signals have been observed in the ultra band of 200–400 nm, which perhaps originate in the $\pi \rightarrow \pi^*$ transitions of $(\text{HL})^{2-}$ ligand. For **1**, positive Cotton effects center at 203 and 224 nm, and negative Cotton effects center at 218 and 295 nm. For **2**, positive Cotton effects center at 205, 223 and 240 nm, and negative Cotton effects center at 217 and 234 nm. The CD spectrum of **3** exhibits positive Cotton effects centered at 203 and 240 nm, and negative Cotton effects centered at 220 and 235 nm. As for **4**, it displays positive Cotton effects centered at 203, 242 and 270 nm, and negative Cotton effects centered at 219 and 249 nm. From the above results, the inherent chirality of H_3L ligand was transmitted to the resulting Ln-HMOFs.

Photoluminescence properties

The lanthanide MOFs usually show excellent luminescent properties. Hence, the photoluminescence of complexes **1–4** and their lifetimes were investigated at room temperature. The excitation spectra for free ligand H_3L and complexes **1–4** are given in Fig. S8–S9.† Upon excitation at 310 nm, the free ligand H_3L exhibits a broad fluorescent emission centered at 369 nm

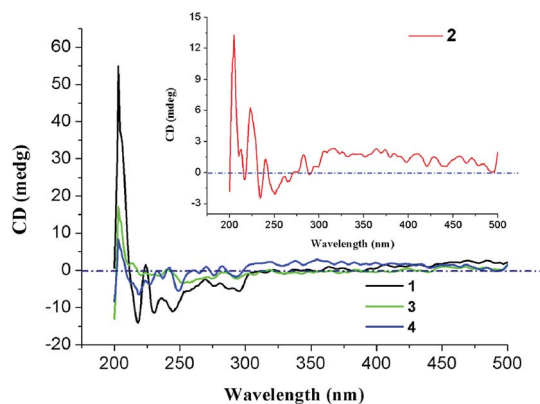


Fig. 4 Solid-state CD spectra of compounds **1–4**.

(Fig. 5a), maybe attributing to intraligand $\pi^* \rightarrow \pi$ charge transfer. Complex **1** presents a broad blue emission centered at 443 nm ($\lambda_{\text{ex}} = 365$ nm) [Fig. 5b], also assignable to the intra-ligand charge transition of $(\text{HL})^{2-}$ ligand. Compared with the emission of free ligand H_3L , the emission peak of **1** red-shifts by 74 nm, indicating obvious influence upon the HOMO and LUMO levels of the coordinated ligand $(\text{HL})^{2-}$ as well as the energy transitions between them owing to the coordination of Gd^{3+} ions. This phenomenon is similar to the previously reported.⁴⁸ The CIE color coordinate is (0.198, 0.214) for **1**. Upon excitation at 395 nm, **2** emits the bright characteristic red color of Eu^{3+} ions with the CIE color coordinate of (0.587, 0.316). The emission peaks at 593, 615, 653 and 701 nm are assigned to $^5\text{D}_0 \rightarrow ^7\text{F}_j$ ($j = 1, 2, 3, 4$) transitions of Eu^{3+} ions, respectively, without the emission peak corresponding to $^5\text{D}_0 \rightarrow ^7\text{F}_0$ transition being observed (Fig. 5c). The electric dipole transition $^5\text{D}_0 \rightarrow ^7\text{F}_2$ dominates the red color emission while the $^5\text{D}_0 \rightarrow ^7\text{F}_1$ transition is insensitive to the site symmetry as a magnetic dipole. For **2** the intensity ratio of $I(^5\text{D}_0 \rightarrow ^7\text{F}_2)/I(^5\text{D}_0 \rightarrow ^7\text{F}_1)$ is about 5.28, indicating that the Eu^{3+} ions locate at a low symmetric coordination environment without an inversion center.^{34,37} This result is in agreement with the crystal structural analysis result that every Eu^{3+} ion adopts a distorted noncentral single-capped square antiprism (C_{4v}) polyhedron configurations (Fig. S6†). Upon excitation at 352 nm, complex **3** exhibits characteristic Tb^{3+} emissions at 490, 545, 586 and 622 nm, which can be attributed to $^5\text{D}_4 \rightarrow ^7\text{F}_j$ ($j = 6, 5, 4, 3$) transitions, respectively (Fig. 5d). The most intense transition of $^5\text{D}_4 \rightarrow ^7\text{F}_5$ leads to strong green luminescence of the crystal sample, which makes **3** become a promising green emitting phosphors with the CIE color coordinate of (0.278, 0.541).

It is worth noting that the ligand-based emission in the fluorescence spectra of compounds **2** and **3** was not observed, indicating effective energy transfer from ligand $(\text{HL})^{2-}$ to the lanthanide centers *via* “antenna effect”. The luminescence decay curves of **1–3** were obtained in the solid state at room

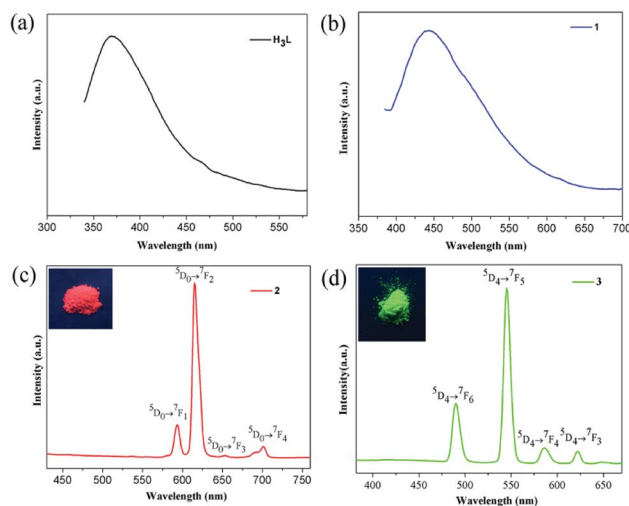


Fig. 5 Solid-state emission spectra of free ligand H_3L (a), **1** (b), **2** (c), and **3** (d) at room temperature. The insets show the corresponding luminescence pictures under UV-light irradiation at 365 nm.



temperature (Fig. S10–S12†). Complexes **1–3** display the single-exponential luminescent decay with the lifetimes of 9.88, 352.95 and 826.26 μ s, respectively, and the quantum yields Φ_{overall} are 3.9% for complex **2** and 5.2% for complex **3**, respectively. When excited at 365 nm at room temperature, compound **4** displays blue photoluminescence mainly originating from the intra-ligand charge transition of $(\text{HL})^{2-}$ ligand (Fig. S9†).

Tuning of luminescent color for bimetallic doped Eu/Tb-HMOFs

The isostructuralism of the resulting Ln-HMOFs **1–4** gives a chance to synthesize heterometallic frameworks by codoping. A series of bimetallic doped Eu/Tb-HMOFs $[(\text{Eu}_x\text{Tb}_{1-x})_2(\text{HL})_2(\text{H}_2\text{O})_4] \cdot 2\text{Cl} \cdot 5\text{H}_2\text{O}$ were successfully obtained by adjusting different molar ratios of Eu^{3+} and Tb^{3+} reactants, and the molar ratio of Eu^{3+} and Tb^{3+} ions was determined by means of ICP spectroscopy (Table S1†).

As shown in Fig. 6a, the bimetallic doped Eu/Tb-HMOFs exhibit the dual emissions of Eu^{3+} and Tb^{3+} ions in their luminescent spectra when excited at 370 nm. With the increase of $\text{Eu}^{3+}/\text{Tb}^{3+}$ molar ratios, the emission intensity of Tb^{3+} at

545 nm ($^5\text{D}_4 \rightarrow ^7\text{F}_5$) decreases monotonically, while that of Eu^{3+} at 615 nm ($^5\text{D}_0 \rightarrow ^7\text{F}_2$) increases stepwise to reach a maximum when the mole fraction of Eu^{3+} is 29.23 mol%, and then decreases slightly due to the concentration quenching effect.^{17,49} The observation suggests the enhanced probability of energy transfer from Tb^{3+} to Eu^{3+} with the increase of Eu^{3+} concentration.^{15,17,19,49} Furthermore, the fluorescence decay of the $^5\text{D}_4 \rightarrow ^7\text{F}_5$ transition of Tb^{3+} and the $^5\text{D}_0 \rightarrow ^7\text{F}_2$ transition of Eu^{3+} in the bimetallic doped samples of $[(\text{Eu}_x\text{Tb}_{1-x})_2(\text{HL})_2(\text{H}_2\text{O})_4] \cdot 2\text{Cl} \cdot 5\text{H}_2\text{O}$ ($x = 14.88\text{--}38.51$ mol%) was also investigated. The results show that with the increase of Eu^{3+} doping, the obtained effective lifetime of Tb^{3+} shortens while that of Eu^{3+} basically increases (Table S3 and Fig. S13†), which indicates that the concentration of doped Eu^{3+} significantly changes the fluorescent dynamics of Tb^{3+} and further confirm an efficient energy transfer from Tb^{3+} to Eu^{3+} . Notably, the lifetime of Eu^{3+} also reaches a maximum when the mole fraction of Eu^{3+} is 29.23 mol%, and then shortens slightly with the further increase of Eu^{3+} doping, reflecting the above mentioned concentration quenching effect. In addition, the observed energy transfer between Tb^{3+} and Eu^{3+} also confirms that the as-synthesized bimetallic doped compounds are single-phase coordination polymers where Eu^{3+} has been successfully incorporated into the lattice of **3** because the energy transfer could not occur in a mixture of separated phases.

Interestingly, the bimetallic doped Eu/Tb-HMOFs present a wide range of visible emission colors such as green, yellow, orange, orange-red, and red under UV-light irradiation at 365 nm (Fig. 6b), indicating that the luminescent colors of the bimetallic doped Eu/Tb-HMOFs $[(\text{Eu}_x\text{Tb}_{1-x})_2(\text{HL})_2(\text{H}_2\text{O})_4] \cdot 2\text{Cl} \cdot 5\text{H}_2\text{O}$ can be systematically modulated through adjusting different mole fractions of Tb^{3+} and Eu^{3+} . At the same time, with the change of the concentration of the doping Eu^{3+} in the heterometallic frameworks, the corresponding CIE chromaticity coordinates change from (0.325, 0.468) to (0.470, 0.287) (Fig. 6b and Table S4†).

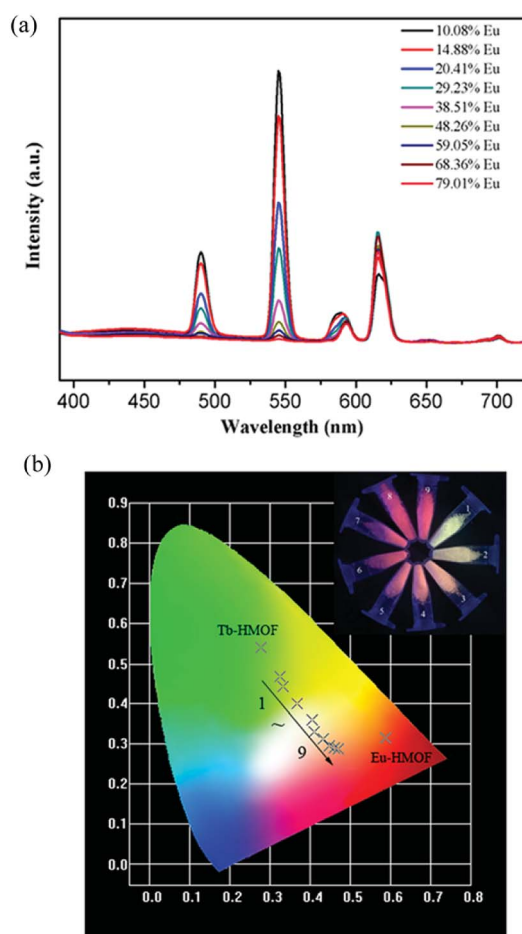


Fig. 6 (a) Solid-state emission spectra of the bimetallic Eu/Tb-HMOFs $[(\text{Eu}_x\text{Tb}_{1-x})_2(\text{HL})_2(\text{H}_2\text{O})_4] \cdot 2\text{Cl} \cdot 5\text{H}_2\text{O}$ when excited at 370 nm ($x = 10.08\text{--}79.01$ mol%); (b) the CIE chromaticity diagram for Eu-HMOF (**2**), Tb-HMOF (**3**), and the bimetallic doped Eu/Tb-HMOFs. The inset shows the luminescence picture of the bimetallic doped Eu/Tb-HMOFs under UV-light irradiation at 365 nm.

WLED for trimetallic doped Eu/Gd/Tb-HMOF

Being considered as fourth-generation light sources, white-light-emitting diodes (WLEDs) have greatly attracted current interest owing to extensive applications in displays and lighting. Isostructural compounds **1**, **2** and **3**, as observed above, exhibit blue, red and green primary colors, respectively, which is expected that white light emission could be obtained by the doping of Eu^{3+} and Tb^{3+} ions into the Gd^{3+} compound **1**. Indeed, the emission output of Eu/Gd/Tb-HMOFs can be controlled precisely through the compositional adjustment of the three metal ions. By optimizing the molar ratio of Eu^{3+} , Gd^{3+} and Tb^{3+} ions, the trimetallic doped Eu/Gd/Tb-HMOF $[(\text{Eu}_{0.1388}\text{Gd}_{0.6108}\text{Tb}_{0.2504})_2(\text{HL})_2(\text{H}_2\text{O})_4] \cdot 2\text{Cl} \cdot 5\text{H}_2\text{O}$ was synthesized successfully. Upon excitation at 370 nm, this three-component compound simultaneously shows the triple emissions originating from the emissions of Eu^{3+} , Tb^{3+} and the coordinated ligand $(\text{HL})^{2-}$, respectively (Fig. 7a), and its CIE color coordinate is (0.285, 0.298). Furthermore, we have systematically studied the subtle effects of excitation



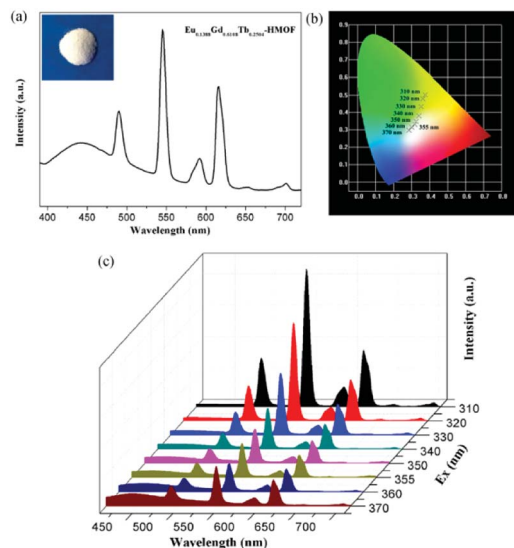


Fig. 7 (a) Solid-state emission spectra of the trimetallic doped Eu/Gd/Tb-HMOF $[(\text{Eu}_{0.1388}\text{Gd}_{0.6108}\text{Tb}_{0.2504})_2(\text{HL})_2(\text{H}_2\text{O})_4] \cdot 2\text{Cl} \cdot 5\text{H}_2\text{O}$ when excited at 370 nm (the inset shows the corresponding luminescence picture under UV-light irradiation at 365 nm); (b) the CIE-1931 chromaticity diagram for the trimetallic doped Eu/Gd/Tb-HMOF with excitation wavelengths varying from 310 to 370 nm; (c) solid-state emission spectra of the trimetallic doped Eu/Gd/Tb-HMOF with excitation wavelengths varying from 310 to 370 nm.

wavelength changes upon the luminescent color of the trimetallic doped Eu/Gd/Tb-HMOF (Fig. 7b and c). As shown in Fig. 6b, when the excitation wavelength is controlled from 310 to 370 nm, the emission color of the trimetallic doped Eu/Gd/Tb-HMOF changes from yellow to white (CIE coordinates in Table S5[†]). The white emission of the trimetallic doped Eu/Gd/Tb-HMOF has been obtained upon excitation at 355 nm [the CIE color coordinate is (0.317, 0.331); the average lifetime values for Tb^{3+} and Eu^{3+} ions are 753.59 and 473.03 μs , respectively (Fig. S14[†]), and the overall quantum yield is about 4.2%,], which is very close to that of pure white light (0.333, 0.333) according to 1931 CIE coordinate diagram. The colour rendering index (CRI) and corresponding colour temperature (CCT) are 82 and 6261 K, respectively, which satisfy the necessary conditions for high quality white light-emitting materials (CRI above 80 and CCT in the range of 2500–6500 K). Although the quantum yield value is smaller than that of several recent trimetallic doped 3D Eu/Gd/Tb-MOFs,^{15,19} studies on 2D Ln-HMOFs as multicolor luminescence materials are fewer at present.

Luminescent sensing of metal ions

To research the potential of Tb-HMOF for sensing of metal ions, the ground samples of the as-synthesized Tb-HMOF were dispersed in aqueous solutions of $\text{M}(\text{NO}_3)_x$ ($\text{M}^{x+} = \text{Na}^+, \text{K}^+, \text{Ag}^+, \text{Cd}^{2+}, \text{Ba}^{2+}, \text{Mg}^{2+}, \text{Mn}^{2+}, \text{Ni}^{2+}, \text{Zn}^{2+}, \text{Cu}^{2+}, \text{Co}^{2+}, \text{Hg}^{2+}, \text{Pb}^{2+}, \text{Fe}^{3+}, \text{Al}^{3+}$, and Cr^{3+}), and handled with ultrasonication treatment for 30 min to form a metal-ion-incorporated Tb-HMOF suspension whose fluorescent measurements were carried out at room temperature upon excited at $\lambda_{\text{ex}} = 352$ nm. As shown in Fig. 8, the incorporated various metal ions exhibit different influences

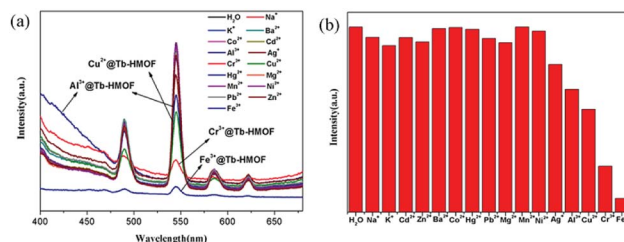


Fig. 8 (a) Emission spectra of Tb-HMOF (10 mg) dispersed in various nitrate salts aqueous solutions (3 mL, 10^{-3} M). (b) Cation selectivity of the Tb-HMOF (I_0/I) in H_2O .

upon the luminescence of Tb^{3+} . For the incorporated $\text{Na}^+, \text{K}^+, \text{Cd}^{2+}, \text{Ba}^{2+}, \text{Mg}^{2+}, \text{Mn}^{2+}, \text{Ni}^{2+}, \text{Zn}^{2+}, \text{Co}^{2+}, \text{Hg}^{2+}$, or Pb^{2+} , the effect on the luminescence intensity at 545 nm of Tb-HMOF is negligible. However, for the incorporated $\text{Ag}^+, \text{Cu}^{2+}, \text{Cr}^{3+}, \text{Al}^{3+}$, or Fe^{3+} , they display different degrees of quenching on the fluorescence of Tb^{3+} with obviously distinguished spectra: $\text{Ag}^+, \text{Al}^{3+}$ or Cu^{2+} has a certain quenching effect on the luminescence intensity, whereas Cr^{3+} or Fe^{3+} has a rapidly quenching effect on the luminescence intensity, and especially for Fe^{3+} it can efficiently and completely quench the emission of Tb^{3+} . In particular, accompanied by the quenching effect on the fluorescence of Tb^{3+} , the incorporated Al^{3+} can largely enhance the ligand-related emission (Fig. 8a). These results suggest that the fluorescence of Tb-HMOF is very sensible to $\text{Fe}^{3+}, \text{Cr}^{3+}$, and Al^{3+} ions, and perhaps has potential application in ion detection.

To further understand the fluorescent sensing behaviours of Tb-HMOF to $\text{Fe}^{3+}, \text{Cr}^{3+}$ and Al^{3+} , concentration-dependent luminescence measurements were carried out. The as-synthesized Tb-HMOF samples were ground and immersed in different concentrations of $\text{Fe}^{3+}, \text{Al}^{3+}$, or Cr^{3+} , and then their luminescence spectra were recorded. As shown in Fig. 9 and S15,[†] the emission intensity of Tb-HMOF suspension is rapidly quenched with increasing concentration Fe^{3+} or Cr^{3+} . When the concentration reaches 5 mM for Fe^{3+} or 30 mM for Cr^{3+} , the luminescence of Tb^{3+} is almost completely quenched.

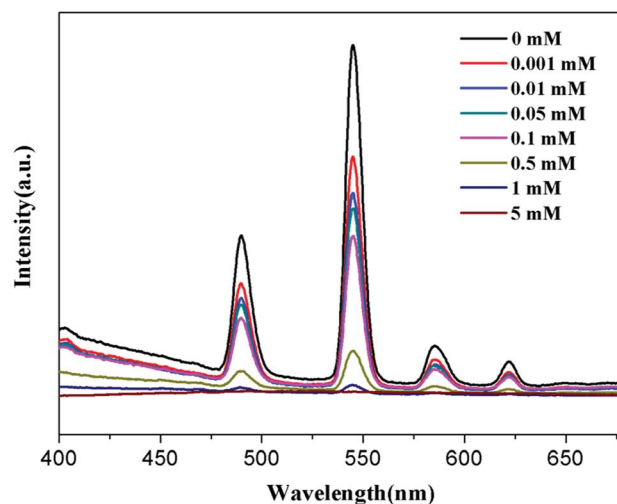


Fig. 9 Emission spectra of Tb-HMOF in aqueous solutions of various concentrations of Fe^{3+} under excitation at 352 nm.



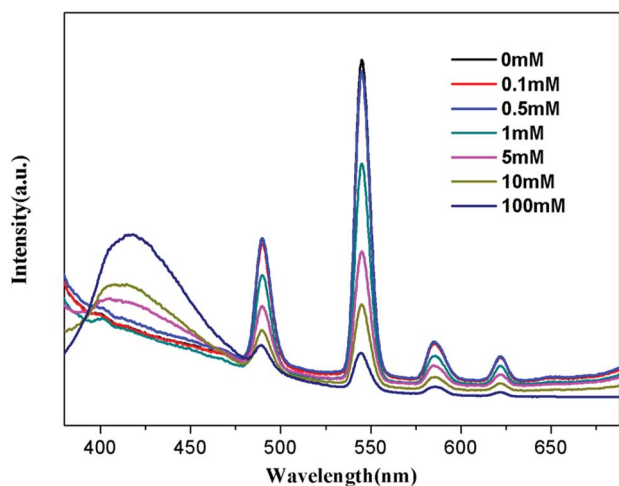


Fig. 10 Emission spectra of Tb-HMOF in aqueous solutions of various concentrations of Al^{3+} under excitation at 352 nm.

Comparatively, the fluorescent quenching effect of Fe^{3+} on the Tb-HMOF is more quick and thorough than that of Cr^{3+} . For the Al^{3+} -incorporated sample, the luminescence intensity of Tb^{3+} decreases slowly and the emission of the ligand-related emission centered at 425 nm increases gradually with increasing concentration Al^{3+} . When the Al^{3+} concentration reaches 10 mM, clear quenching of the luminescence of Tb^{3+} can be seen (Fig. 10). As the concentration of Al^{3+} increases to 100 mM, the luminescence of Tb^{3+} is nearly completely quenched and only the emission of the ligand can be observed. Further with the increase of Al^{3+} concentration, Tb-HMOF dissolves gradually, and finally forms a clear aqueous solution as the Al^{3+} concentration reaches 0.1 M. This phenomenon has been reported in previous literature.⁵⁰

Conclusions

In summary, we have successfully synthesized a series of novel Ln-HMOFs based on chiral ligand (*S*)-5-(((1-carboxyethyl)amino)methyl)isophthalic acid (H_3L). All complexes are isostructural with (3,6)-connected homochiral frameworks whose phase purities and chirality are further confirmed by PXRD and CD studies, respectively. The luminescent investigation of 1–4 suggests that compounds 2 and 3 display the strong characteristic emissions of the corresponding Eu^{3+} and Tb^{3+} ions, while 1 and 4 exhibit blue emissions arising from ligand (HL)²⁻. By doped different Ln^{3+} ions into single-phase Ln-HMOFs, the bimetallic Eu/Tb-HMOFs $[(\text{Eu}_x\text{Tb}_{1-x})_2(\text{HL})_2(\text{H}_2\text{O})_4] \cdot 2\text{Cl} \cdot 5\text{H}_2\text{O}$ and trimetallic Eu/Gd/Tb-HMOF $[(\text{Eu}_{0.1388}\text{Gd}_{0.6108}\text{Tb}_{0.2504})_2(\text{HL})_2(\text{H}_2\text{O})_4] \cdot 2\text{Cl} \cdot 5\text{H}_2\text{O}$ have been successfully fabricated. The emission colors of bimetallic Eu/Tb-HMOFs can be tuned among green, yellow, orange, orange-red, and red by adjusting the doping concentration of Eu^{3+} ions into the Tb-HMOF. Very important, the trimetallic doped Eu/Gd/Tb-HMOF $[(\text{Eu}_{0.1388}\text{Gd}_{0.6108}\text{Tb}_{0.2504})_2(\text{HL})_2(\text{H}_2\text{O})_4] \cdot 2\text{Cl} \cdot 5\text{H}_2\text{O}$ features white light emission upon excitation at 355 nm, whose emission can also be switched between different colors when excited with different ultraviolet light. Furthermore, the fluorescence

response of Tb-HMOF to various usual metal ions, and especially fluorescent sensing behaviours to Fe^{3+} , Cr^{3+} and Al^{3+} has been preliminarily investigated.

Conflicts of interest

The authors declare no competing financial interest.

Acknowledgements

We gratefully acknowledge financial support from the National Natural Science Foundation of China (21271157), and the Foundation and Research in Cutting-Edge Technologies in the Project of Henan Province (122300410092).

Notes and references

- 1 M. Roushan, X. Zhang and J. Li, *Angew. Chem., Int. Ed.*, 2012, **51**, 436–439.
- 2 Y. C. Liao, C. H. Lin and S. L. Wang, *J. Am. Chem. Soc.*, 2005, **127**, 9986–9987.
- 3 P. C. P. Lima, F. A. Almeida Paz, R. A. S. Ferreira, V. De Zea Bermudez and L. S. D. Carlos, *Chem. Mater.*, 2009, **21**, 5099–5111.
- 4 Y. S. Zhao, H. B. Fu, F. Q. Hu, A. D. Peng, W. S. Yang and J. N. Yao, *Adv. Mater.*, 2008, **20**, 79–83.
- 5 G. He, D. Guo, C. He, X. Zhang, X. Zhao and C. Duan, *Angew. Chem., Int. Ed.*, 2009, **48**, 6132–6135.
- 6 Q. Ju, D. Tu, Y. Liu, R. Li, H. Zhu, J. Chen, Z. Chen, M. Huang and X. Chen, *J. Am. Chem. Soc.*, 2012, **134**, 1323–1330.
- 7 J. Rocha, L. D. Carlos, F. A. A. Paz and D. Ananias, *Chem. Soc. Rev.*, 2011, **40**, 926–940.
- 8 A. Schoedel, M. Li, D. Li, M. O'Keeffe and O. M. Yaghi, *Chem. Rev.*, 2016, **116**, 12466–12535.
- 9 J. C. G. Bünzli, *Chem. Rev.*, 2010, **110**, 2729–2755.
- 10 L. D. Carlos, R. A. S. Ferreira, V. De Zea Bermudez, B. Julian-Lopez and P. Escrivano, *Chem. Soc. Rev.*, 2011, **40**, 536–549.
- 11 F. F. Chen, Z. Q. Chen, Z. Q. Bian and C. H. Huang, *Coord. Chem. Rev.*, 2010, **254**, 991–1010.
- 12 J. Heine and K. Muller-Buschbaum, *Chem. Soc. Rev.*, 2013, **42**, 9232–9242.
- 13 H. Jeong, B. Lee, S. Byeon, H. Jeong, B. Lee and S. Byeon, *ACS Appl. Mater. Interfaces*, 2016, **8**, 10946–10953.
- 14 L. Armelao, D. Belli Dell Amico, L. Bellucci, G. Bottaro, L. Labella, F. Marchetti and S. Samaritani, *Inorg. Chem.*, 2016, **55**, 939–947.
- 15 Q. Tang, S. X. Liu, Y. W. Liu, D. F. He, J. Miao, X. Q. Wang, Y. J. Ji and Z. P. Zheng, *Inorg. Chem.*, 2014, **53**, 289–293.
- 16 X. Yang, X. Lin, Y. Zhao, Y. S. Zhao and D. Yan, *Angew. Chem., Int. Ed.*, 2017, **56**, 7853–7857.
- 17 M. L. Ma, C. Ji and S. Q. Zang, *Dalton Trans.*, 2013, **42**, 10579–10586.
- 18 J. Rong, W. Zhang and J. Bai, *RSC Adv.*, 2016, **6**, 103714–103723.
- 19 Y. W. Zhao, F. Q. Zhang and X. M. Zhang, *ACS Appl. Mater. Interfaces*, 2016, **8**, 24123–24130.



- 20 H. Xu, C. S. Cao, X. M. Kang and B. Zhao, *Dalton Trans.*, 2016, **45**, 18003–18017.
- 21 K. X. Shang, J. Sun, D. C. Hu, X. Q. Yao, L. H. Zhi, C. D. Si and J. C. Liu, *Cryst. Growth Des.*, 2018, **18**, 2112–2120.
- 22 Y. Y. An, L. P. Lu, S. S. Feng and M. L. Zhu, *CrystEngComm*, 2018, **20**, 2043–2052.
- 23 Y. Yang, F. L. Jiang, C. P. Liu, L. Chen, Y. L. Gai, J. Pang, K. Z. Su, X. Y. Wan and M. C. Hong, *Cryst. Growth Des.*, 2016, **16**, 2266–2276.
- 24 J. Rong, W. Zhang and J. Bai, *CrystEngComm*, 2016, **18**, 7728–7736.
- 25 K. Kim, J. S. Seo, D. Whang, H. Lee, S. I. Jun, J. Oh and Y. J. Jeon, *Nature*, 2000, **404**, 982–986.
- 26 M. Yoon, R. Srirambalaji and K. Kim, *Chem. Rev.*, 2012, **112**, 1196–1231.
- 27 Y. Liu, W. M. Xuan and Y. Cui, *Adv. Mater.*, 2010, **22**, 4112–4235.
- 28 L. Ma, C. Abney and W. Lin, *Chem. Soc. Rev.*, 2009, **38**, 1248–1256.
- 29 K. K. Bisht, B. Parmar, Y. Rachuri, A. C. Kathalikattil and E. Suresh, *CrystEngComm*, 2015, **17**, 5341.
- 30 Z. G. Gu, C. Zhan, J. Zhang and X. Bu, *Chem. Soc. Rev.*, 2016, **45**, 3122–3144.
- 31 K. Mo, Y. H. Yang and Y. Cui, *J. Am. Chem. Soc.*, 2014, **136**, 1746–1749.
- 32 Z. G. Gu, W. Q. Fu, M. Liu and J. Zhang, *Chem. Commun.*, 2017, **53**, 1470–1473.
- 33 Z. X. Xu, Y. X. Tan, H. R. Fu, J. Liu and J. Zhang, *Inorg. Chem.*, 2014, **53**, 12199–12204.
- 34 Q. Yue, J. Yang, G. H. Li, G. D. Li and J. S. Chen, *Inorg. Chem.*, 2006, **45**, 4431–4439.
- 35 C. H. Gao, L. Zhang, G. F. Hou, D. S. Ma, W. H. Jiang and Y. H. Yu, *Inorg. Chem. Commun.*, 2017, **78**, 70–73.
- 36 L. Sun, G. F. Hou, W. H. Jiang, Q. Huang, Y. H. Yu and J. S. Gao, *Polyhedron*, 2017, **129**, 55–59.
- 37 T. Liu, Y. H. Yu, H. Z. Zhang, W. H. Jiang, J. S. Gao and G. F. Hou, *Cryst. Growth Des.*, 2017, **17**, 1788–1795.
- 38 X. Wang, K. Zhang, L. Lv, R. Chen, W. Wang and B. Wu, *Cryst. Growth Des.*, 2018, **18**, 1799–1808.
- 39 H. S. Jang, H. Yang, S. W. Kim, J. Y. Han, S. G. Lee and D. Y. Jeon, *Adv. Mater.*, 2008, **20**, 2696–2702.
- 40 Y. Lu and B. Yan, *Chem. Commun.*, 2014, **50**, 15443–15446.
- 41 G. N. Wysocki and W. S. Stiles, *Color Science: Concepts and Methods, Quantitative Data, and Formulae*, John Wiley & Sons, New York, Wiley classics library edn, 2000.
- 42 G. M. Sheldrick, *SADABS, Program for Empirical Absorption Correction of AreaDetector Data*, University of Göttingen, Göttingen, Germany, 1997.
- 43 G. M. Sheldrick, *SHELXS-97, Program for X-ray Crystal Structure Determination*, University of Göttingen: Göttingen, Germany, 1997.
- 44 G. M. Sheldrick, *SHELXS-97, Program for X-ray Crystal Structure Refinement*, University of Göttingen: Göttingen, Germany, 1997.
- 45 A. L. Spek, *J. Appl. Crystallogr.*, 2003, **36**, 7–13.
- 46 B. Wu, S. Wang, R. Wang, J. Xu, D. Yuan and H. Hou, *Cryst. Growth Des.*, 2013, **13**, 518–525.
- 47 J. P. Costes, T. Yamaguchi, M. Kojima and L. Vendier, *Inorg. Chem.*, 2009, **48**, 5555–5561.
- 48 Z. J. Li, X. Y. Li, Y. T. Yan, L. Hou, W. Y. Zhang and Y. Y. Wang, *Cryst. Growth Des.*, 2018, **18**, 2031–2039.
- 49 K. Liu, H. You, Y. Zheng, G. Jia, Y. Song, Y. Huang, M. Yang, J. Jia, N. Guo and H. Zhang, *J. Mater. Chem.*, 2010, **20**, 3272–3279.
- 50 L. H. Cao, F. Shi, W. M. Zhang and S. Q. Zang, *Chem.–Eur. J.*, 2015, **21**, 15705–15712.

